

An Updated Index Including Toughness for Hot-Cracking Susceptibility



GUANNAN TANG, BENJAMIN J. GOULD, ABIGAIL NGOWE,
and ANTHONY D. ROLLETT

Hot cracking is one of the major defects that can occur in laser-based additive manufacturing. During the terminal stage of solidification, hot cracking initiates when the semi-solid matrix builds up excessive negative (tensile) pressure induced by thermal contraction. This study presents a new quantification of the trends in the above process: we estimate the volume change brought by thermal deformation through a perspective of energy conservation and combine it with the intergranular volume change induced by grain growth and liquid backflow to derive a criterion for hot-cracking initiation. Based on this, we propose two modified indexes that build on prior work, namely: (1) $\left| \frac{dT}{df_s} \right| \frac{1}{\sqrt{1-\beta}}$ and (2) $\left| \frac{dT}{df_s} \right| \frac{1}{\bar{E}}$. Here, T is temperature, f_s is the solid fraction of the semi-solid region, β is the shrinkage factor and \bar{E} is the material toughness near the solidus temperature. Evaluating these indexes against experimental data reveals that hot-cracking susceptibility is strongly correlated with the second index and indeed is a function of material high-temperature toughness.

<https://doi.org/10.1007/s11661-022-06612-6>

© The Minerals, Metals & Materials Society and ASM International 2022, corrected publication 2022

I. INTRODUCTION

HOT cracking is notoriously common in both laser- and electron beam-based additive manufacturing, as well as casting of many commercial alloys (e.g., Al 6061,^[1, 2] Al7075,^[3] Haynes 230^[4] and Inconel 738^[5]). It is a serious defect that is a direct cause of part rejection and can degrade the mechanical performance of fabricated parts. Hot cracking often occurs in the semi-solid matrix of solidifying welds, also known as the mushy zone. The coexistence of solid dendrites with liquid makes the behavior of this mushy zone complex. The center line of the melt pool in welding or laser powder bed fusion (LPBF) is the last to solidify and so this is often the critical location for initiation of cracking. Liquid metal can flow continuously and easily into the semi-solid skeleton at low solid fractions. Regions of the mushy zone close to the solidus, however, have a high fraction of solid, and the dendrites in this region form solid linkages between each other. This connectivity gives the matrix strength and also obstructs the flow of liquid melt that compensates for solidification

shrinkage. As the solid fraction approaches unity, the remaining liquid forms films between the dendrites such that liquid flow is constrained or even blocked. At the same time, the semi-solid structure develops strength that resists thermal shrinkage thereby setting up tensile stress; thus, the inter-dendritic spots where voids can nucleate.^[6] When the accumulated strain exceeds the mechanical limit, the liquid melt film will be pulled apart leaving behind a voided space that can serve as the initiation spot for hot cracking. This is the mechanism that is often credited in the literature with causing the terminal stage of solidification to be critical for hot-cracking initiation.^[7]

Even though the initiation of hot cracking in welding can be generalized to be a net result of competing events within the mushy zone during solidification, the alloy itself has a strong influence on the occurrence or severity of hot cracking in welding. The freezing range of the alloy, defined as the difference between liquidus temperature and solidus temperature, is strongly correlated with hot-cracking susceptibility.^[8] The wider the freezing range, the longer the material will spend in the vulnerable, semi-solid, state, thereby promoting cracking.^[9] Solute segregation also influences the local freezing range. In nickel alloys, the segregation of solute can lower the local solidus temperature and extend the freezing range further, potentially leading to an increase in the hot-cracking susceptibility.^[9] Moreover, grain size of the alloy also affects the formation of hot cracks. This is saying that any process condition influencing the final grain texture can have an effect on the eventual

GUANNAN TANG, ABIGAIL NGOWE, and ANTHONY D. ROLLETT are with the Department of Materials Science and Engineering, Carnegie-Mellon University, Pittsburgh, PA 15213. Contact e-mail: rollett@andrew.cmu.edu. BENJAMIN J. GOULD is with the Applied Materials Division, Argonne National Laboratory, Lemont, IL 60490.

Manuscript submitted September 5, 2021; accepted January 21, 2022.

hot-cracking behavior. Alloys with finer grains are generally less susceptible to hot cracking.^[10] Finer grains allow more movement between adjacent grains and consequently are better at accommodating thermal contraction.^[11] In addition, fine-grained materials have more intergranular area per unit volume. This results in higher intergranular liquid permeability and less localized solute segregation, therefore, promoting the “healing” effect of liquid backflow and, at the same time, reducing solute segregation.

Indeed, hot cracking is a notably complex phenomenon that depends on aspects that are often interrelated. Attempts have already been made in the literature to unify those aspects. As reviewed by Eskin,^[12] criteria for hot cracking can be categorized into three types: critical stress, critical strain, and critical strain-rate. The stress-based criteria focus on the mechanical strength of the solid network (mushy zone). This type of criterion assumes that a crack will form when the local thermal tensile stress exceeds the network’s mechanical strength. The strain-based studies use a similar approach by assuming that a crack will form when the local tensile strain is sufficient to pull apart a grain boundary and fracture the continuous liquid/solid network. More recent studies suggest that strain rate, more than stress and strain, may play a dominant role in the formation of a hot crack.^[6] The basis for this view is that, in the course of solidification, stress relief occurs via a combination of liquid backfeed and diffusional creep in response to thermal shrinkage, both of which are time dependent. Although the semi-solid network can fail from a large enough stress or strain, hot cracks do not occur if enough time is available for stress relaxation. This view is consistent with the known high strain-rate sensitivity of plastic deformation at high temperature, e.g., Reference 13.

Prokhorov’s work is, to the best of our knowledge, the first report that analyzes the significance of strain rate.^[14] He asserted that there is a threshold for the rate of strain accumulation with temperature drop. Hot cracks can occur if this threshold is exceeded during solidification. A more elaborate model, also based on strain-rate, is the oft-cited RDG model proposed by Rappaz, Drezet, and Gremaud.^[15] This model simplifies the problem to that of unidirectional columnar grain growth with a liquid backfeed in the opposite direction. Using a differential mass-balance equation between the grain growth and liquid back feed, the RDG model relates the pressure drop along the grain boundary to the local thermal deformation and solidification shrinkage. The maximum allowable pressure drop is defined by the critical cavitation (tensile) pressure. If the solidification-induced pressure drop exceeds this maximum allowable value, a void may form and eventually give rise to a crack. More recently, Kou proposed a related approach that models hot cracking at the scale of an individual grain boundary instead of the mushy zone as a whole.^[16] Using the same volume balance among the thermal deformation, grain growth, and the liquid backfeed, Kou related the extent of hot-cracking susceptibility with $|dT/d(f_s)^{1/2}|$ at the terminal stage of

solidification (solid fractions in a range from 85 pct to 92 pct). Here, f_s is the solid fraction within the mushy zone during solidification, and T is the local temperature. Larger values of $|dT/d(f_s)^{1/2}|$ represent a higher hot-cracking susceptibility. This agrees well with the fact that alloys with large freezing ranges are known to be more susceptible to hot cracking. However, discrepancies remain. Among commercial Al alloys, for example, Kou has pointed out himself that back-diffusion must be included to make a correct cracking susceptibility prediction when Al 5052 is compared to Al 6061.^[17] Also, predictions from Kou’s analysis failed to correlate well with experimental data for certain Ni alloys.^[18]

The purpose of the current work is to extend Kou’s index to address the discrepancies seen in various alloys. Accordingly, we propose a numerical analysis of the criterion for the initiation of hot cracking within the mushy zone. However, rather than only limiting the analysis to the volumetric balance within the intergranular region, the relaxation of strain energy by plastic deformation at the terminal stage of solidification is considered in the current work, from which several factors are extracted and incorporated into Kou’s index to extend its capability. Experimental data are used to evaluate the different indices and find the most effective modification to the original index and, more importantly, validate the hot-cracking model proposed in this work.

II. MATERIALS AND METHODS

A. Dynamic X-ray Radiography (DXR)

DXR is a characterization technique that utilizes the large X-ray flux afforded by synchrotron radiation sources to provide extremely high temporal fidelity images of high-speed interactions, such as the LPBF process. The current work utilizes a system developed at the 32-ID-B beamline of Advanced Photon Source (APS) at Argonne National Laboratory to study LPBF.^[19] APS, as a third-generation light source provides high-speed synchrotron X-ray radiation that is able to penetrate samples with high temporal and spatial resolution. This makes DXR a powerful tool for studying the melting and solidification processes of laser welding. The schematic of the setup is shown in Figure 1. The specimen is placed in an environment of

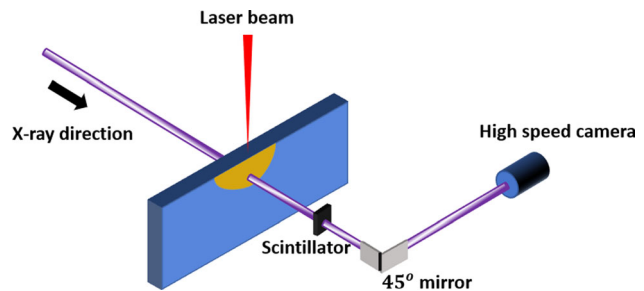


Fig. 1—Schematic of the dynamic X-ray radiography experiment setup.

argon atmosphere and kept at room temperature. The laser beam interacts with the specimen from the top surface while the X-ray penetrates through the whole specimen from the front surface. The density change during melting creates changes in the X-ray absorption. Using a high-speed camera to view the image of the transmitted X-rays on a scintillator reveals the time-resolved evolution of the melt pool dynamics, which makes the in-situ characterization of the hot-cracking morphology possible. A typical frame rate is 50 kHz, but much higher rates are possible. In our work, DXR is used to examine the morphology of the hot-cracking network in a set of four aluminum alloys and six Ni-based alloys. To optimize the X-ray absorption contrast, the aluminum specimens were prepared with dimensions about 50 mm long, 3 mm tall, and 1 mm thick. Because of their higher density, the Ni-based specimens were prepared with the same dimensions but only 0.5 mm thick.

B. Derivation of Hot-Cracking Susceptibility Indexes

Motivated by Kou's approach, we consider the grain growth at the terminal stage of solidification shown in Figure 2, two columnar grains are growing next to each other. λ is the grain spacing and L is the grain radius. Note that the cross section shows the top view of the grain growth. The empty space in the cross section outlined by hexagons is the intergranular space where hot cracking is likely to initiate. Along this intergranular channel, volume balance is maintained by compensating the volume change induced by thermal deformation with the net volume change resulting from grain growth and liquid backflow. In our current model, we specifically investigated a small section of the intergranular channel. This small cross section is indicated by the dotted orange rectangle that has width w and extends in the vertical direction along the intergranular channel with height Δh .

Within this control volume, initiation of hot cracking can be avoided when the rate of volume opening up by thermal deformation (V_{thermal}) is smaller than the compensation rate of volume change from liquid backflow (V_{liquid}) and grain growth (V_{growth}):

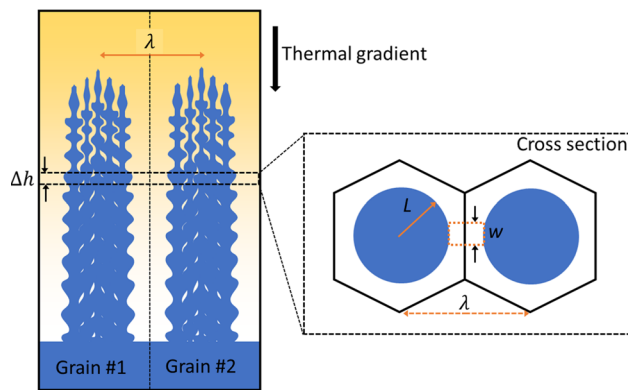


Fig. 2—A schematic for the top view of an intergranular channel.

$$\frac{dV_{\text{thermal}}}{dt} < \frac{dV_{\text{liquid}}}{dt} + \frac{dV_{\text{growth}}}{dt}. \quad [1]$$

Assume the reference height of this controlled volume is h , we can rewrite Inequality (1) according to Kou's work^[16] as follows:

$$\frac{dV_{\text{thermal}}}{dt} < w * \Delta h * \frac{d2L}{dt} + (w * (\lambda - 2L) * v_l|_{(h+\Delta h)} - w * (\lambda - 2L) * v_l|_h). \quad [2]$$

Here, $w * \Delta h * \frac{d2L}{dt}$ on the right-hand side describes the volume compensation rate brought by grain growth. The last two terms on the right-hand side correspond to the volumetric flow rate of the liquid melt that goes in and out of the controlled volume. The difference between these two terms gives the volume compensation rate induced by fluid backflow. Here, $v_l|_h$ and $v_l|_{(h+\Delta h)}$ are the liquid flow speed at vertical position h and $h + \Delta h$, respectively. By dividing Δh on both sides and taking the limit of $\Delta h \rightarrow 0$, the volume Inequality (2) can be rewritten as follows:

$$\frac{dV_{\text{thermal}}}{dh * dt} < w * \frac{d(2L)}{dt} + w * \frac{d(\lambda - 2L)v_l}{dh} |_h. \quad [3]$$

As reported by Kou,^[16] L can be expressed as a function of λ and local solid fraction f_s when f_s approaches 1.

$$L = \frac{\lambda}{2} \sqrt{1 - \beta} \sqrt{f_s}. \quad [4]$$

Here β is the solidification shrinkage coefficient ($\beta = 1 - \frac{\rho_s}{\rho_l}$). Substitute Equation (4) into Inequality (3) and divide by λ and w on both sides:

$$\frac{dV_{\text{thermal}}}{w * \lambda * dh * dt} < \sqrt{1 - \beta} \frac{d\sqrt{f_s}}{dt} + \frac{d(1 - \sqrt{1 - \beta} \sqrt{f_s})v_l}{dh} |_h \quad [5]$$

The first term $\frac{dV_{\text{thermal}}}{w * \lambda * dh}$ in inequality (5) describes the rate of volume fraction change or strain rate of thermal deformation in our controlled volume. If we evaluate the initiation of hot cracking from an energy perspective, then the strain energy stored in the material that is relaxed by void or crack creation that compensates for the energy consumed in local plastic deformation and the increase in surface energy as new surface is created during the initiation of a hot crack. Plastic deformation is brought about by stress caused by thermal shrinkage. By analogy with the Griffith criterion^[20] for brittle cracking (extended to include plasticity), we evaluate the energy conservation of this process:

$$U_{\text{strain}} = E_{\text{plastic}} * V_{\text{plastic}} + \gamma * C_{\text{plastic}}. \quad [6]$$

Here U_{strain} is the strain energy. E_{plastic} is the energy per unit volume consumption for plastic fracture, and γ is the surface energy of the material. V_{plastic} is the volume deformed by thermal stress and C_{plastic} is the surface area created during the initiation of a hot crack. In general, the energy consumed in creating new

surface is orders of magnitude smaller than that consumed in plastic deformation.^[21] Accordingly, we rewrite Eq. [6] as follows:

$$U_{\text{strain}} = E_{\text{plastic}} * V_{\text{plastic}}. \quad [7]$$

We can use Eq. [7] to estimate the volume of plastically deformed material induced by thermal stress. Plugging it into Inequality [5] to replace V_{thermal} , we obtain

$$\frac{dU_{\text{strain}}}{E_{\text{plastic}} * w * \lambda * dh * dt} < \sqrt{1 - \beta} \frac{d\sqrt{f_s}}{dt} + \frac{d(1 - \sqrt{1 - \beta}\sqrt{f_s})v_l}{dh} |h. \quad [8]$$

Here, E_{plastic} is treated as a material property and is estimated as being proportional to material toughness \bar{E} , *i.e.*, the area under the stress-strain curve. Since strain hardening is negligible close to the melting point, toughness can be approximated as the product of yield (flow) stress multiplied by the strain to failure. Rearranging Inequality [8] with a transformation of the solidification shrinkage term $\frac{d\sqrt{f_s}}{dt} = \left(\frac{dT}{dt} \div \frac{dT}{d\sqrt{f_s}}\right)$:

$$\frac{dU_{\text{strain}}}{w * \lambda * dh * dt} < \bar{E} * \left(\sqrt{1 - \beta} \left(\frac{dT}{dt} \div \frac{dT}{d\sqrt{f_s}} \right) + \frac{d(1 - \sqrt{1 - \beta}\sqrt{f_s})v_l}{dh} |h \right). \quad [9]$$

Inequality [9] gives a quantitative requirement for avoiding hot-cracking initiation. It connects the microscopic phenomena of grain growth and liquid backfeed to the macroscopic material properties, *i.e.*, material toughness (\bar{E}). To eliminate hot-cracking initiation, inequality [9] must be satisfied. Note that the term $\frac{dT}{d\sqrt{f_s}}$ that appears on the right side of inequality [9] is the original index proposed by Kou,^[16] Increasing the value of this index will lead to a decrease on the right of Inequality [9], meaning that there will be less compensation by deformation and consequently increased hot-cracking susceptibility. This is in agreement with Kou's analysis. Moreover, the prefactors on the right-hand side of inequality [9] also influence the balance of this inequality: First, $\sqrt{1 - \beta}$ represents the ratio of the material density at liquidus and solidus temperatures. The smaller this ratio (*i.e.*, the greater the departure from unity), the more severe the solidification shrinkage that the material undergoes, and therefore,

the greater the susceptibility to hot cracking. This is apparent in Inequality [9] in that increasing this term decreases the right-hand side. Secondly and similarly, \bar{E} in Inequality [9] represents the high-temperature toughness of the material. The smaller this term, the more easily plastic fracture occurs and, in turn, initiation of hot cracking. This is evident in that decreasing the value of \bar{E} leads to a decrease on the right-hand side of Inequality [9], meaning that again there will be less compensation by plasticity and, as a result, the system will be more susceptible to hot cracking. To better evaluate the effect of the two prefactors, we incorporate them separately into Kou's original index and obtain two different versions of the modified hot-cracking susceptibility index:

$$\text{Index1 : } \left| \frac{dT}{d\sqrt{f_s}} \right| \cdot \frac{1}{\sqrt{1 - \beta}}$$

$$\text{Index2 : } \left| \frac{dT}{d\sqrt{f_s}} \right| \cdot \frac{1}{\bar{E}}$$

C. Evaluation of the Hot-Cracking Susceptibility Index

The two modified indexes are compared with two independent datasets: (1) DXR data and (2) literature-derived data. The relevant compositions of all the alloys appeared in these two datasets are summarized in Tables I, II, and III in Appendix A. The first dataset used the post-solidification DXR images of 10 alloys (Al5052, Al6061, Al2024, Al7075, Haynes 120, Haynes X, Haynes 160, Haynes 718, Haynes 214, and Haynes 230). The area associated with hot cracking was counted on each image, see Section III-A, and taken to be representative of the extent of hot-cracking susceptibility. Ranking these obtained pixel area counts provides a rank ordering of hot-cracking susceptibility of those 10 alloys, which is then used to evaluate our two modified indexes. The second dataset was extracted from the literature.^[8,18,22] The first paper reports on the hot-cracking susceptibility of six Al alloys (Al2017, Al2219, Al5052, Al5083, Al6061, and Al 7075). The second paper reports on testing of six Ni alloys (Haynes 282, Haynes HR120, Haynes 718, Haynes 230, Haynes 214, and Haynes HR160). The third and last reference discusses the well-known WRC-1992 curve which describes quantitatively how the Cr/Ni composition ratio in austenitic stainless steel is related to hot-cracking susceptibility (shown in Figure 3). Five austenitic

Table I. Chemical Compositions for Al Alloys in This Work

Pct (Wt)	Si	Fe	Cu	Mn	Mg	Cr	Zn	Ti	Zr	V	B	Al
A2017	0.53	0.19	3.89	0.62	0.55	0.11	0.05	0.02	—	—	—	Rest
A2219	0.06	0.16	6.05	0.26	—	—	0.01	0.04	0.14	0.09	—	Rest
A2024	0.1	0.2	4.2	1.3	1.5	0.06	0.13	0.09	—	—	—	Rest
A5052	0.06	0.13	0.01	0.02	2.54	0.21	—	0.01	—	—	—	Rest
A5083	0.14	0.19	0.04	0.67	4.57	0.13	0.01	0.03	—	—	0.0012	Rest
A6061	0.71	0.16	0.18	0.03	0.97	0.08	0.03	0.02	—	—	—	Rest
A7075	0.1	0.19	1.64	0.0001	2.62	0.19	5.62	0.02	—	—	—	Rest

Table II. Chemical Compositions for Ni Alloys in This Work

Pct (Wt)	Cr	Co	Mo	Ti	Al	Fe	C	Mn	Si	B	Nb	Cu	W	Y	Zr	Ni
HAYNES X	21.27	1.55	8.59	0.01	0.12	18.63	0.07	0.51	0.24	0.002	0.1	—	0.59	—	—	Rest
HAYNES 282	20.0	10.0	8.5	2.1	1.5	1.5	0.06	0.3	0.15	0.005	—	—	—	—	—	Rest
HAYNES HR120	25.0	2.5	2.5	—	0.1	33.0	0.05	0.7	0.6	0.004	0.7	—	2.5	—	—	Rest
HAYNES 718	18.4	—	3.0	0.9	0.5	19.0	0.05	0.1	0.1	0.004	5.1	0.15	—	—	—	Rest
HAYNES 230	21.85	0.19	1.21	0.01	0.38	1.48	0.1	0.51	0.12	—	—	—	14.0	—	—	Rest
HAYNES 214	16.0	0.15	0.1	0.1	4.4	3.6	0.04	0.17	0.2	0.003	0.03	—	0.1	0.01	0.003	Rest
HAYNES HR160	28.3	30.8	0.05	0.53	0.09	0.1	0.05	0.45	2.67	—	0.05	—	—	—	—	Rest

Table III. Chemical Compositions for Stainless Steels in This Work

Pct (Wt)	C	Mn	P	S	Si	Cr	Ni	N	Ti	Mo	Fe
321	0.08	2.0	0.045	0.03	0.75	19.0	12.0	0.1	0.7	—	Rest
316	0.08	2.0	0.045	0.03	0.75	18.0	14.0	0.1	—	3	Rest
309S	0.08	2.0	0.045	0.03	0.75	24.0	16.0	—	—	—	Rest
310S	0.08	2.0	0.045	0.03	1.5	26.0	22.0	—	—	—	Rest
304	0.08	2.0	0.045	0.03	1.0	20.0	10.5	—	—	—	Rest

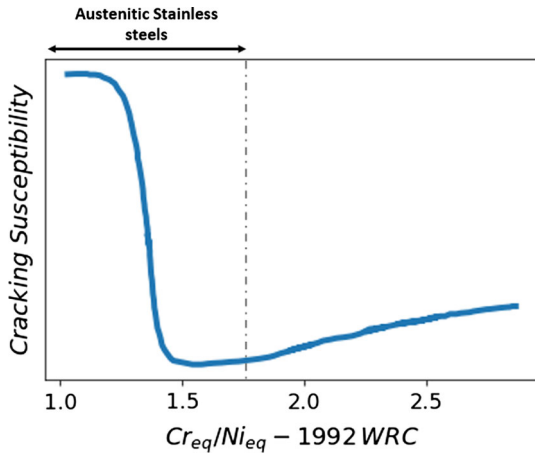


Fig. 3—Adapted from Ref. [8], the WRC-1992 curve that delineates the relationship between Cr/Ni composition ratio in austenitic stainless steel and hot-cracking susceptibility.

stainless steels (321, 316, 309S, 310S, 304) were evaluated in this case. The data from all three sources were ranked from the highest hot-cracking susceptibility to the least and were used to validate the results from the DXR dataset (first dataset).

Computing the value of the modified index for each alloy in the evaluation involves calculating $\left| \frac{dT}{d\sqrt{f_s}} \right|$, $\sqrt{1-\beta}$, and \bar{E} separately. The value of $\left| \frac{dT}{d\sqrt{f_s}} \right|$ was determined by plotting the curve of T vs. $f_s^{1/2}$ and finding the average value of the curve slope over the terminal stage ($0.89 < f_s < 0.98$), which was readily implemented using the Scheil module package from the commercially available software Thermo-Calc.^[23] Similarly, we used Thermo-Calc to compute the material's molar volume

evolution during solidification, which was converted into density evolution and used to compute the value of $\sqrt{1-\beta}$. For the last term \bar{E} , we estimated it by extracting high-temperature tensile test data from the literature^[24-30] for all the surveyed Al alloys. Note that the high-temperature tensile test data for stainless steels and Ni alloys were obtained from the property specifications provided by two commercial companies: (1) North American Stainless and (2) Haynes International, respectively. Since the stress-strain curves at high temperature (near the solidus temperature) generally show negligible strain hardening, we estimated \bar{E} as the product of the yield strength and fracture elongation, as mentioned above.

To quantify the performance of the modified indexes, hot-cracking susceptibility rank predictions of those surveyed alloys based on the calculated values of the modified indexes were made and compared with experimental rankings obtained from the DXR dataset and the literature dataset. Spearman's rank-order correlation coefficient was used here for quantifying the correlations. This coefficient measures the strength and direction of the association between two ranked variables. It calculates the average distance between the compared variables in the hyper-dimensional space. A simplified formula for it is given by

$$r_s = 1 - \frac{6 \sum d_i^2}{n(n^2 - 1)}. \quad [10]$$

Here r_s is the Spearman rank-order correlation coefficient, d_i is the distance between the i^{th} paired observation and n is the total number of observations. This expression gives r_s a range of [-1,1]. Negative values of this coefficient indicate an inverse correlation, whereas positive values represent a positive correlation. In this work, the predictions of hot-cracking susceptibility rank and the corresponding experimental validation are

treated as two different variables. A good prediction must have a positive coefficient which indicates a strong positive correlation.

III. RESULTS

A. Experimental Ranking of the Hot-Cracking Susceptibility

1. DXR dataset

DXR images of the final hot-cracking network were collected for all ten aluminum and nickel alloys at two processing conditions: (1) laser power of 520 W and laser scan speed of 0.2 m/s, and (2) laser power of 520 W and laser scan speed of 0.3 m/s. Detailed information for using DXR test to capture laser welding process can be found in Appendix A. An example of the DXR images is shown in Figure 4(a). The red-shaded regions outline

the hot-cracked area and, by counting the pixel area of all the hot-cracked regions, we obtained a measure of the hot-cracking susceptibility from each DXR experiment. Figure 4(b) shows a bar plot of the extracted hot-cracking susceptibility for all ten alloys. Notice that the relative rankings of the hot-cracking pixel area are the same in both processing conditions, and we generalized them as a single ranking of the hot-cracking susceptibility for all ten alloys:

(DXR dataset ranking)

Al7075 > Al6061 > Al2024 > Al5052 > 230 .
> 160 > X > 120 > 214 > 718

2. Literature dataset

For validation, we took the Vareststraint test results from Kazuhiro,^[22] Watson,^[18] and the WRC-1992 curve

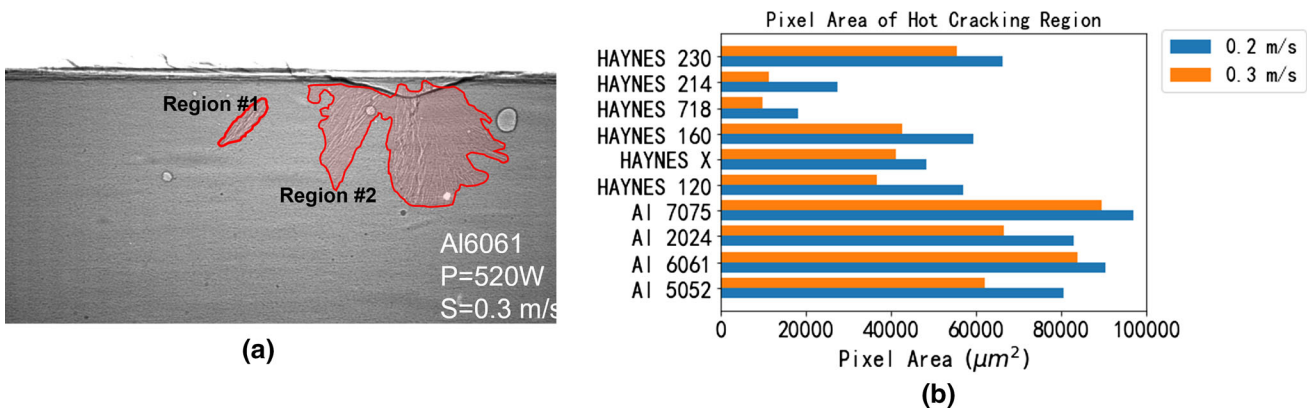


Fig. 4—(a) A DXR image of the final hot-cracking network for Al6061 laser melted at 520W and 0.3 m/s (b) Hot-cracking pixel area values for all ten alloys surveyed.

Table IV. The Extracted High-Temperature Tensile Behavior of 12 Alloys

	Flow Stress (MPa)	Elongation to Fracture	Test Temperature ($^{\circ}\text{C}$)	Strain Rate (/s)
A2017	55	0.19	400	0.005
A2219	21	0.79	400	0.01
A2024	26.4	0.59	400	0.01
A5052	137	0.44	300	0.083
A5083	72	0.71	340	0.01
A6061	21	0.46	450	0.01
A7075	53	0.48	350	0.01
HAYNES X	65	0.5	1093	0.000083
HAYNES 282	129	0.61	982	0.000083
HAYNES HR120	91	0.75	982	0.000083
HAYNES 718	67	1.76	982	0.000083
HAYNES 230	69	0.37	1093	0.000083
HAYNES 214	10	1.34	1204	0.000083
HAYNES HR160	14	0.91	1204	0.000083
312	25	0.87	1100	ISO 6892-2
316	25	0.76	1204	ISO 6892-2
309S	25	0.72	1204	ISO 6892-2
310S	45	0.57	1204	ISO 6892-2
304	20	0.96	1204	ISO 6892-2

as specified in the Methods section. Hot-cracking susceptibility results for six Al alloys, six Ni alloys, and five stainless steels were extracted and converted into susceptibility rankings. Note that Kazuhiro's work used electron beam welding and a fixed welding speed of 16.7 mm/s. This is different than the Vareststraint test setting chosen in Watson's work where laser welding with 400 W and 25 mm/s were used. Lastly, the WRC-1992 curve is a data-driven approach that is based on the prediction of ferrite content. All this means that inter-comparison among these three data sets is not necessarily meaningful. Thus, instead of a single generalized rank, we obtained three susceptibility ranks for each of the Al alloys, Ni alloys, and stainless steels, respectively. All the analysis will be based on each group separately.

- (Literature1) Al6061 > Al2017 > Al7075 > Al2219 > Al5052 > Al5083
- (Literature2) 160 > 120 > 230 > 718 > 214 > 282
- (Literature3) 321 > 316 > 304 > 309S > 310

The high-temperature tensile behavior from the literature of all the alloys examined in this work is summarized in Table IV in Appendix A. The calculated high-temperature material toughness \bar{E} is shown in Figure 5. Note that, owing to the scarcity of published high-temperature tensile data, the test data were extracted at a test temperature of approximately 150°C and 100°C below the corresponding solidus temperatures for the nickel and aluminum alloy groups respectively. For the stainless steels, 300°C below the solidus temperature was chosen. Test strain rates were set at the manufacturer's standard for the Ni alloy and stainless steel groups (See details in Table IV), and at 0.01 m/s for the Al alloy group. For this reason, all the evaluations were done separately for the three different alloy groups. The solidification path (T vs. $f_s^{1/2}$) of each alloy was calculated with Thermo-Calc. The results are plotted in Figures 6(a), (b), and (c). Averaging the slope of the curve over the range of ($0.89 < f_s < 0.98$), we obtained the value of $\left| \frac{dT}{d\sqrt{f_s}} \right|$ for each alloy. This is shown in Figures 6(d),

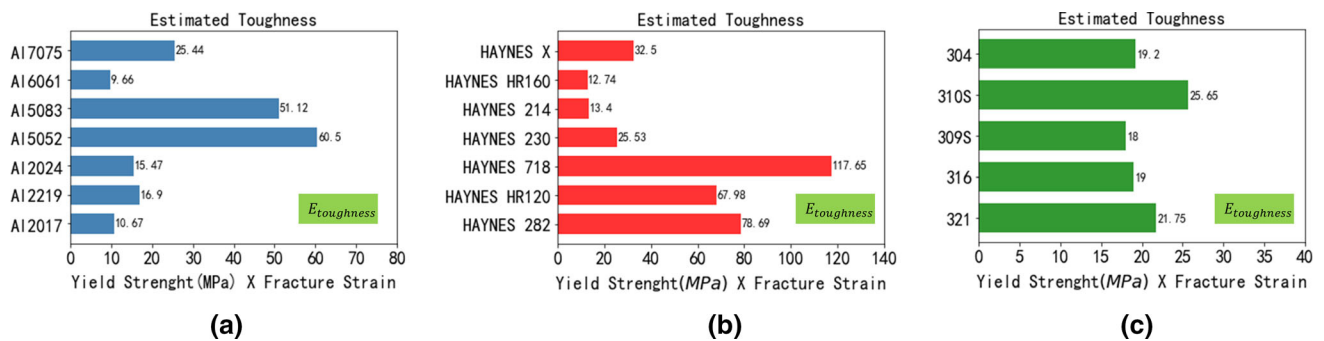


Fig. 5—Calculated values of high-temperature material toughness \bar{E} for (a) Al alloys, (b) Ni alloys, and (c) Stainless steels, respectively.

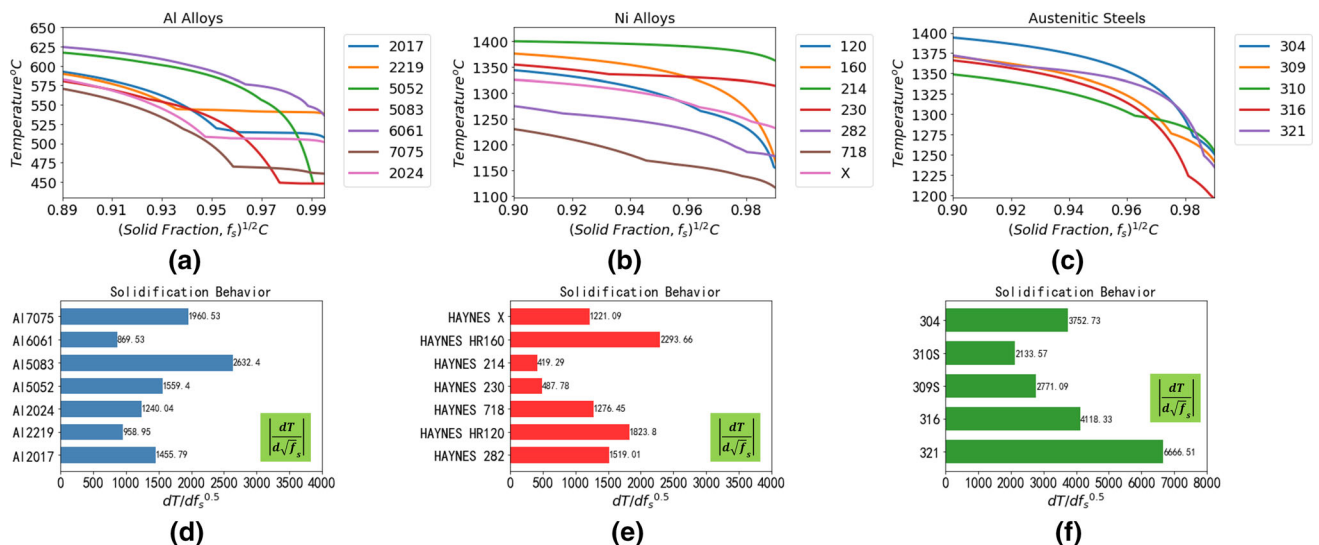


Fig. 6—Calculated solidification path for (a) Al alloys, (b) Ni alloys, and (c) Stainless steels and the average slope values for (d) Al alloys, (e) Ni alloys, and (f) Stainless steels.

(e), and (f). Similarly, we used Thermo-Calc to compute the molar volume change during solidification and converted it into the ratio between liquidus

density and solidus density, which is shown in Figure 7(a) for Al alloys, Figure 7(b) for Ni alloys, and Figure 7(c) for stainless steel.

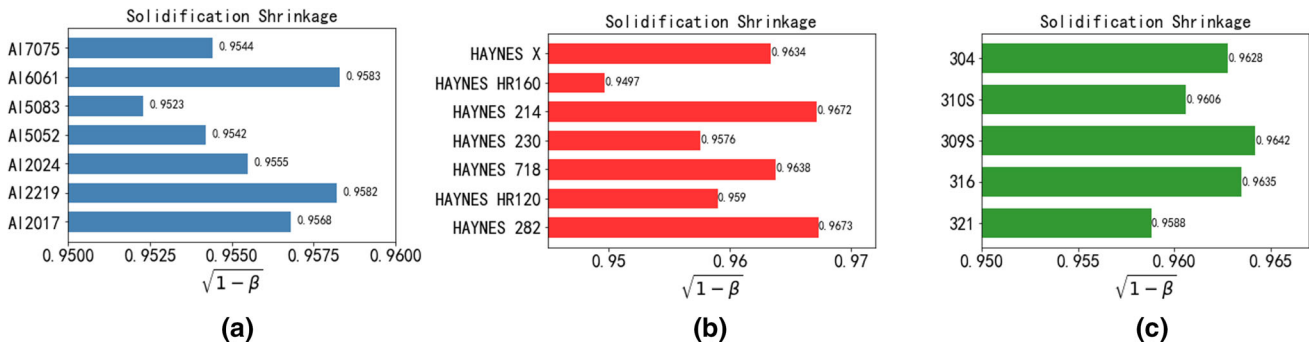


Fig. 7—Calculated solidification shrinkage term $\sqrt{1-\beta}$ for (a) Al alloys, (b) Ni alloys, and (c) Stainless steels, respectively.

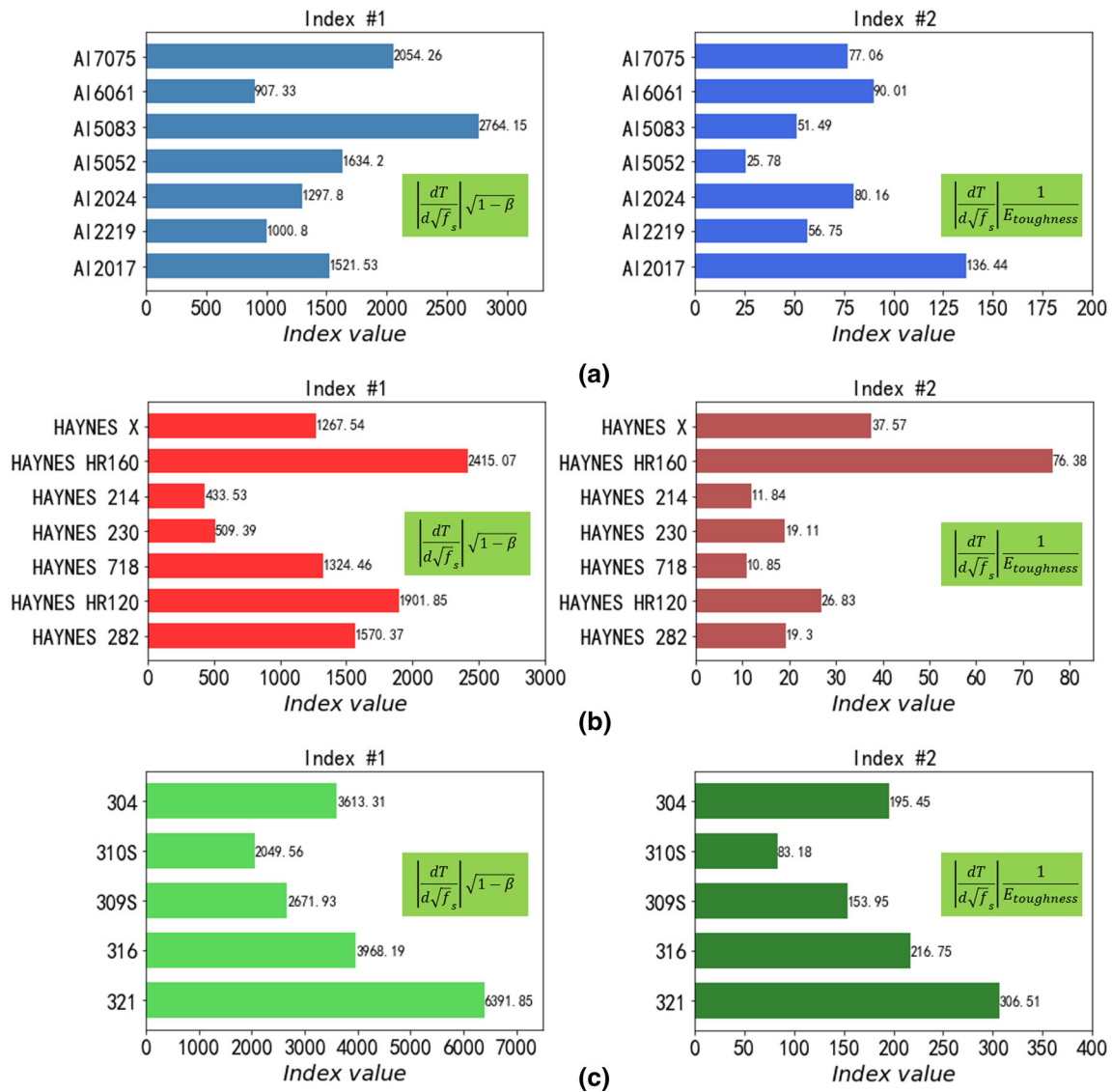


Fig. 8—Calculated values of the two modified indexes for (a) Al alloys, (b) Ni alloys, and (c) stainless steels, respectively.

B. Prediction of Hot-Cracking Susceptibility

Combining the shrinkage term shown in Figure 7 with the average value of the solidification behavior shown in Figure 6, we obtained the values for our first susceptibility index $\left| \frac{dT}{d\sqrt{f_s}} \right| \cdot \sqrt{1-\beta}$. Similarly, combining high-temperature materials toughness, as shown in Figure 5, with the solidification behavior term, we obtained the values for our second susceptibility index $\left| \frac{dT}{d\sqrt{f_s}} \right| \cdot \frac{1}{E}$. Those are given in Figure 8 for Al alloys, Ni alloys, and Stainless steels, respectively.

As a comparison, we also calculated the values of Kou's original index here. In his recent work, the susceptibility index is represented as the maximum slope value at the terminal portion of T vs. $f_s^{1/2}$ plot (Specifically, Al alloys and stainless steels were evaluated over $0.9 < f_s^{1/2} < 0.99$ ^[31, 32] and Ni alloys were evaluated over $0.9 < f_s^{1/2} < 0.98$ ^[33] According to the solidification path that we obtained from Thermo-Calc (Figures 6(a), (b) and (c)), the maximum slopes for all surveyed alloys are summarized in Figure 9.

We start the evaluation with our DXR dataset. As mentioned above, the high-temperature toughness data from literature were tested under the different conditions for our surveyed Al group alloys and Ni group alloys. For this reason, our evaluation then was separated into two groups: (1) Al test group (Al7075, Al6061, Al2024, and Al5052) and (2) Ni test group (230, 160, X, 120, 214, and 718). For index 1 $\left| \frac{dT}{d\sqrt{f_s}} \right| \cdot \frac{1}{\sqrt{1-\beta}}$, we have

$$\begin{aligned} (\text{Altestgroup}) & 7075 > 5052 > 2024 > 6061 \\ (\text{Nitestgroup}) & 160 > 120 > 718 > X > 230 > 214 \end{aligned}$$

Similarly, for index 2 $\left| \frac{dT}{d\sqrt{f_s}} \right| \cdot \frac{1}{E}$, we have

$$\begin{aligned} (\text{Altestgroup}) & 6061 > 2024 > 7075 > 5052 \\ (\text{Nitestgroup}) & 160 > X > 120 > 230 > 214 > 718 \end{aligned}$$

The results of using Spearman's rank-order correlation to evaluate the above rankings against the experimental rankings from the DXR dataset are summarized in Table V. We find that Index 2 gives the best prediction in both the Al and Ni test groups with $r_s = 0.4$ for Al test group and $r_s = 0.6571$ for Ni test group. By contrast, Index 1 yielded the lowest coefficient values with $r_s = 0.2$ for Al test group and $r_s = 0.0857$ for Ni test group.

As a baseline comparison, Kou's original index predicted:

$$\begin{aligned} (\text{Altestgroup}) & 5052 > 7075 > 6061 > 2024 \\ (\text{Nitestgroup}) & 160 > 120 > X > 718 > 214 > 230 \end{aligned}$$

These yielded coefficient values with $r_s = -0.2$ for the Al test group and $r_s = 0.0286$ for the Ni test group.

Validation was performed with the literature data as mentioned above.^[8,18,22] Based on the surveyed alloys' data in Figure 8, we obtained the following susceptibility rank predictions for Index 1:

$$\begin{aligned} (\text{Al test group}) & \text{Al5083} > \text{Al7075} > \text{Al5052} > \text{Al2017} \\ & > \text{Al2219} > \text{A6061} \\ (\text{Ni test group}) & 160 > 120 > 282 > 718 > 230 > 214 \\ (\text{Stainless steel test group}) & 321 > 316 > 304 > 309S > 310S \end{aligned}$$

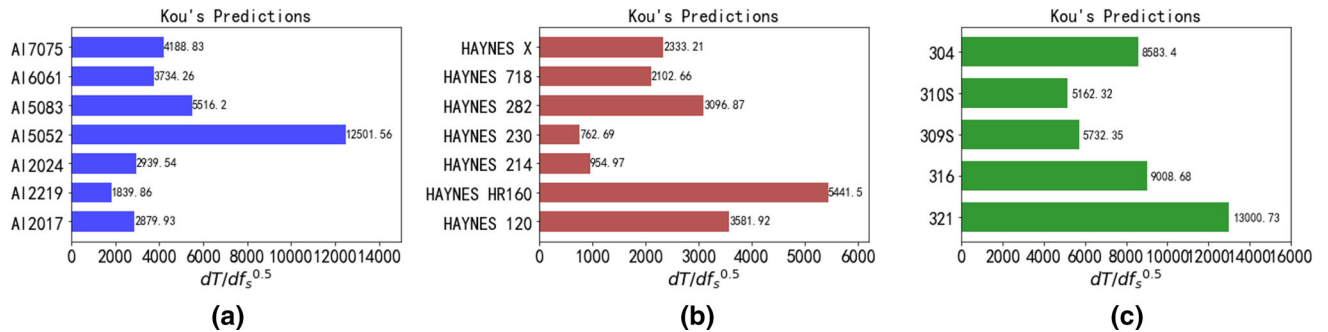


Fig. 9—Hot-cracking susceptibility prediction based on Kou's original index for (a) Al alloys, (b) Ni alloys and (c) Stainless steels.

Table V. Computed Spearman's Rank-Order Coefficient for All Three Indexes

	DXR dataset		Literature dataset		
	Al group	Ni group	Al group	Ni group	Steel group
Index 1	0.2000	0.0857	-0.7143	0.6000	1
Index 2	0.4000	0.6571	0.8857	0.6000	1
Kou's Index	-0.2000	0.0286	-0.5429	0.4857	1

Similarly, the predictions from Index 2 are as follows:

(Al test group) Al2017 > Al6061 > Al7075 > Al2219
> A5083 > A5052
(Ni test group) 160 > 120 > 282 > 230 > 214 > 718
(Stainless steel test group) 321 > 316 > 304 > 309S > 310S

Again, we used Spearman's rank-order correlation to evaluate our index rankings against the experimental rank from the literature dataset. The results are also summarized in Table V. Here, we find that Index 2 still provides the best prediction with $r_s = 0.8857$ for Al test group and $r_s = 0.6$ for Ni test group. Index 1 reached $r_s = -0.7143$ for Al test group and $r_s = 0.6$ for Ni test group. By contrast, Index 1 and Index 2 both gave $r_s = 1$ for steel test group, and so, they cannot be distinguished from each other.

For comparison, Kou's original index predicts

(Kou's prediction on Al test group) Al5052 > A5083
> A7075 > A6061 > A2017 > A2219
(Kou's prediction on Ni test group) 160 > 120 > 282
> 718 > 214 > 230
(Kou's prediction on steel test group) 321 > 316 > 304
> 309S > 310S

Calculation of the correlation coefficient yielded $r_s = -0.5429$ for the Al test group, $r_s = 0.4857$ for the Ni test group, and $r_s = 1$ for the steel test group.

IV. DISCUSSION

As it is evident in Table V, the stainless steel test group shows perfect correlation for all three tested indexes. This is mainly a result of the limited data size of the steel test group and partly because of the scarcity of high-temperature tensile test data. For this reason, Kou's original method yielded a correlation coefficient of 1 for the current steel test group, i.e., it is equally successful so there is nothing to be gained in modifying Kou's index with toughness or solidification shrinkage. Fortunately, the incorporation of toughness or solidification shrinkage into the hot-cracking susceptibility index does not result in a negative impact on the prediction. Consequently, the rest of the discussion focuses on the Al and Ni alloys where the correlation difference before and after the index modification is more apparent.

Direct comparison among rank predictions and experimental results in Table V reveals that Index 2 made the best prediction for both the DXR and literature datasets. Note that, except for the result of Al group in DXR dataset, the calculated Spearman's coefficients for Index 2 are all above or at least equal to 0.6. This indicates that a positive correlation exists between the hot-cracking susceptibility and Index 2, meaning that the prediction made from this index is more similar to the experimental measurement in terms of the rank order and, thus, has a better accuracy. As for

the rather small coefficient value in Al group of the DXR dataset for Index 2, we point out that there are only four test alloys considered in this group owing to the limited DXR experiment time and the scarcity of suitable high-temperature tensile data. As a result of this, even a single false prediction in the rank order of hot-cracking susceptibility results in a large penalty when we evaluate the predictions against the experimental data with Spearman's rank-order correlation. It is more appropriate to just compare this test group result across all three alloys rather than use it as a correlation benchmark. From this perspective, Index 2 exhibits the highest value of Spearman's rank-order coefficient among the three and remains the best index even when the dataset size is small.

Regarding Index 1, it does not represent much of an improvement over Kou's original index. This is mainly because the differences in solidification density change are minimal across all the surveyed alloys (shown in Figure 7). This implies that it might help to explore models that would magnify these subtle differences. To do this, however, more data will be needed to carry out a parameter optimization, which is left for future study. Similarly, the current size of our total dataset remains too small to use more sophisticated machine learning algorithms such as Random Forest. As for the baseline, the highest value of Kou's index was 0.4857 and for the other alloy groups, Kou's index exhibited a non-positive correlation with the experimental ranking. This shows that Kou's index lacks generality when applied to a broader spectrum of materials, which is not surprising because Kou's index only considers the solidification behavior of the alloy. As pointed out in the introduction, even though the initiation of hot cracking is largely controlled by the competing events within the mushy zone and depends strongly on the solidification behavior of the material, there are other factors that also play an important role in the formation of hot cracking. The better performance of Index 2 over Kou's index is notable here and is mainly a result of incorporating high-temperature material toughness, as originally suggested by Reference 14. Incorporating material toughness into the index takes into account the mechanical properties of the mushy zone. At the terminal stage of the solidification, the presence of thermal strain, solidification shrinkage and insufficient liquid backflow are necessary but not sufficient conditions for hot cracking to initiate in welds. If the local dendritic microstructure has enough mechanical toughness to accommodate the thermal contraction and the resulting tensile stretch, the low pressure region can relax sufficiently to avoid initiating a crack. We conclude that the initiation of hot cracking depends on materials toughness at high temperatures, which also explains why, as shown in Figure 4(b), all the Ni-based alloys exhibit less hot-cracking susceptibility than the Al alloys. It also helps explain why the Varestraint test enjoys the popularity that it does in the welding community despite the challenges of converting the data into a material property.

It is worth noting that some of the false predictions made from Index 2 may be because of the scarcity of high-temperature tensile data available in the literature.

The phenomenon of hot cracking mostly happens during the process of solidification, which means the local temperature of hot-cracking spot should be around solidus temperature. In our work, we used the tensile test data obtained at 150 °C (Ni alloy group), 100 °C (Al alloy group) and 300 °C (Stainless steel group) below the corresponding solidus temperature, respectively. Knowing that alloys can have widely different responses to temperatures near solidus line, tensile data that are representative of behavior close to the solidus temperature are likely to be more relevant to the hot-cracking phenomenon. More accurate high-temperature data on mechanical properties should enable more accurate prediction of hot cracking.

V. CONCLUSIONS

We present a new analysis of the hot-cracking susceptibility based on rank correlation and conclude that both solidification characteristics and high-temperature mechanical behavior are significant. Given the challenges of quantifying hot cracking as a property and the limited data available, we computed rank correlation coefficients for multiple alloy types between two new indexes of materials properties and multiple types of experimental data. We modified Kou's original index to include solidification density change $\left| \frac{dT}{d\sqrt{f_s}} \right| \cdot \frac{1}{\sqrt{1-\beta}}$ as the first index and material toughness at high temperature $\left| \frac{dT}{d\sqrt{f_s}} \right| \cdot \frac{1}{E}$ as the second index. Evaluation of these two indexes was conducted with both direct experimental data from synchrotron-based high-speed visualization of cracking and literature data. The second index $\left| \frac{dT}{d\sqrt{f_s}} \right| \cdot \frac{1}{E}$ gave the best prediction with values of Spearman's rank-order coefficient greater than 0.6 in most cases, which indicates positive correlations between the predictions made from this index and the experimental data. The prediction of hot-cracking susceptibility was improved when the second index $\left| \frac{dT}{d\sqrt{f_s}} \right| \cdot \frac{1}{E}$ is compared with Kou's index.^[16] This supports the idea that the hot-cracking susceptibility is also a function of high-temperature toughness even though its influence is not apparent in certain alloy systems (such as stainless steels). By contrast, the first index $\left| \frac{dT}{d\sqrt{f_s}} \right| \cdot \frac{1}{\sqrt{1-\beta}}$ did not perform any better than Kou's index and does not offer any improvement in the prediction of hot cracking.

ACKNOWLEDGMENTS

The authors acknowledge support from the National Science Foundation under Grant number DMR-1905910. This research used resources of the Advanced Photon Source, a U.S. Department of Energy (DOE) Office of Science User Facility operated for the DOE

Office of Science by Argonne National Laboratory (ANL) under Contract No. DE-AC02-06CH11357 in addition to support through Laboratory Directed Research and Development (LDRD) funding from ANL under the same contract. The authors are indebted to the 32-ID beamline staff scientists, notably Kamel Fezzaa, Tao Sun, Cang Zhao, and Niranjana Parab for assistance with running the DXR experiments. Additional, we would like to give our thanks to Prof. Robert Suter who helped a lot with organizing our latex code.

CONFLICT OF INTEREST

The authors declare that they have no conflict of interest.

APPENDIX A

Figure 10 gives a detailed time series demonstration of a DXR test capturing the evolution of laser welding in Al 6061 under the processing condition of 520 W and 0.3 m/s. The melt pools were outlined in red-dotted line. Figures 10(a) and (b) captures two moments during the welding process where the laser was scanning from the left to the right. Figure 10(c) captures the moment where the laser was turned off at the end. We can see that the melt pool shrunk in Figure 10(d) and became fully solidified in Figure 10(e). The crack bundles are quite visible in Figure 10(e). To demonstrate reproducibility, we took the DXR test on Al 2024 samples and examined under the spot welding condition for simplicity where a laser power of 520 W and the laser dwell time of 2 s were used. Using this condition, a series of spot welding DXR results were obtained and are shown in Figure 11. Figures 11(a), (b), (c), and (d) is taken from one sample but from different spots. Figures 11(e), (f), (g), and (h) is taken from a different sample and is also obtained at different spots. Note that, even though DXR images in Figure 11 were obtained at two different samples and different spots, the observed final crack bundles in each image share a great similarity with each other. This supports the reproducibility of DXR test and can be used as a valid method to examine hot-cracking susceptibility.

Table IV summarizes the details of the high-temperature tensile test results that we used from literature to compute the material toughness for all 12 alloys. Notice that, for the stainless steel group, the exact strain-rate values used for testing the tensile properties were not shown here because they were not provided in the original data source. However, it was provided that all 5 stainless steels were tested under the same international standard EN 6892-2,^[34] which still makes it durable to make comparison analysis within the stainless steel group.

Tables I, II, and III summarize the chemical compositions of all the alloys in Table IV. Those composition values were used in Thermo-Calc to calculate the

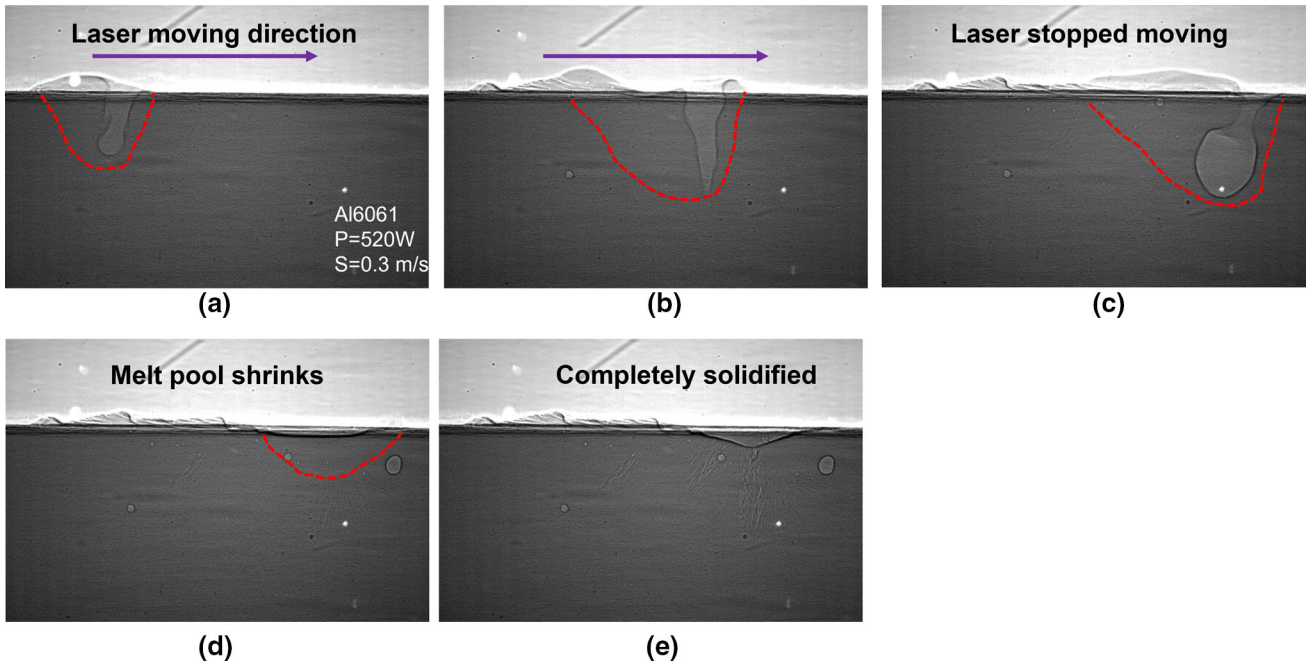


Fig. 10—The evolution of laser-welding process captured by a series of DXR images: (a) the start of the welding, (b) the middle of the welding, (c) laser off, (d) solidifying, and (e) fully solidified, respectively.

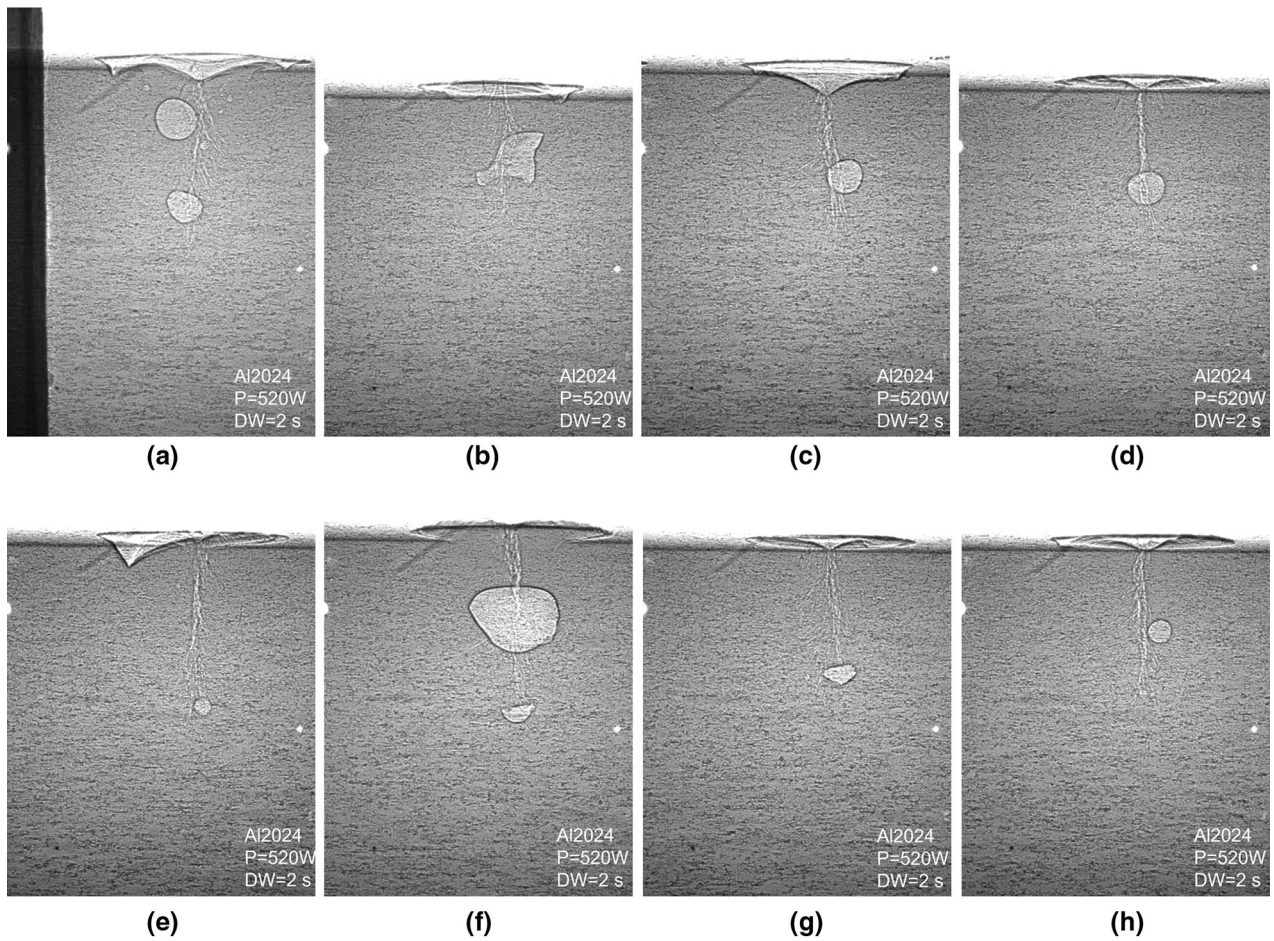


Fig. 11—Spot-welding DXR results from sample one shown in (a),(b),(c), and (d); Spot-welding DXR results from sample two shown in (e),(f),(g), and (h).

corresponding solidification behavior and solidification density change of all the surveyed alloys here.

REFERENCES

1. C.E. Roberts, D. Bourell, T. Watt, and J. Cohen: A novel processing approach for additive manufacturing of commercial aluminum alloys. *Phys. Procedia*, vol. 83, pp. 909–917. *Laser Assisted Net Shape Engineering 9 International Conference on Photonic Technologies Proceedings of the LANE 2016*, September 19–22, 2016 Fürth, Germany, 2016.
2. S.Z. Uddin, D. Espalin, J. Mireles, P. Morton, C. Terrazas, S. Collins, L.E. Murr, and R. Wicker: Laser powder bed fusion fabrication and characterization of crack-free aluminum alloy 6061 using in-process powder bed induction heating. In *Solid Freeform Fabrication 2017: Proceedings of the 28th Annual International Solid Freeform Fabrication Symposium—An Additive Manufacturing Conference, SFF 2017*, 2020, pp. 214–27.
3. N. Kaufmann, M. Imran, T.M. Wischeropp, C. Emmelmann, S. Siddique, and F. Walther: Influence of process parameters on the quality of aluminium alloy en AW 7075 using Selective Laser Melting (SLM). In *Physics Procedia*, 2016, Elsevier B.V., vol. 83, pp. 918–26.
4. C.M. Cheng, C.P. Chou, I.K. Lee, and I.C. Kuo: *J. Mater. Sci. Technol.*, 2006, vol. 22(5), pp. 685–90.
5. X. Zhang, H. Chen, L. Xu, J. Xu, X. Ren, and X. Chen: *Mater. Des.*, 2019, vol. 183, p. 12.
6. D.G. Eskin, Suyitno, and L. Katgerman, *Prog. Mater. Sci.*, 2004, 49, 629–711.
7. N. Hatami, R. Babaei, M. Dadashzadeh, and P. Davami: *J. Mater. Process. Technol.*, 2008, vol. 205(1–3), pp. 506–13.
8. J.C. Lippold and D.J. Kotecki: *Welding Metallurgy and Weldability of Stainless Steels*, Wiley, Hoboken, 2005.
9. R. Thavamani, V. Balusamy, J. Nampoothiri, R. Subramanian, and K.R. Ravi: *J. Alloys Compd.*, 2018, vol. 740, pp. 870–78.
10. M. Saadati and A.K.E. Nobarzad: *J. Manuf. Process.*, 2019, vol. 41, pp. 242–51.
11. H. Zhang, H. Zhu, X. Nie, J. Yin, Z. Hu, and X. Zeng: *Scr. Mater.*, 2017, vol. 134, pp. 6–10.
12. D.G. Eskin and L. Katgerman, *Metall. Mater. Trans. A: Phys. Metall. Mater. Sci.*, 2007, vol. 38 A, pp. 1511–19.
13. T.H. Courtney: *Mechanical Behavior of Materials*, McGraw-Hill, Boston, 2000.
14. N.N. Prokhorov: *Russ. Cast. Prod.*, 1962, vol. 2(2), pp. 172–75.
15. M. Rappaz, J.M. Drezet, and M. Gremaud, A new hot-tearing criterion. Technical Report 2, 1999.
16. S. Kou: *Acta Mater.*, 2015, vol. 88, pp. 366–74.
17. J. Liu, H.P. Duarte, and S. Kou: *Acta Mater.*, 2017, vol. 122, pp. 47–59.
18. J.S. Watson, Fiber laser weldability of austenitic nickel alloys. Technical report, 2017.
19. C. Zhao, K. Fezzaa, R.W. Cunningham, H. Wen, F. De Carlo, L. Chen, A.D. Rollett, and T. Sun: *Sci. Rep.*, 2017, vol. 7(1), pp. 1–11.
20. L.G. Margolin: *Eng. Fract. Mech.*, 1984, vol. 19(3), pp. 539–43.
21. D. Roylance, *Introduction to Fracture Mechanics*. Massachusetts Institute of ..., Department of Materials Science and Engineering, 2001.
22. K. Nakata and F. Matsuda: *Q. J. Jpn. Weld. Soc.*, 1995, vol. 13(1), pp. 106–15.
23. J.-O. Andersson, T. Helander, L. Hdghmd, P. Shi, and B. Sundman, Thermo-Calc & DICTRA, computational tools for materials science. Technical Report–2, 2002.
24. E. Vaghefi and S. Serajzadeh, *Met. Mater. Int.*, 2020.
25. K. Shojaei, S.V. Sajadifar, and G.G. Yapici: *Mater. Sci. Eng. A.*, 2016, vol. 670, pp. 81–89.
26. T. Gan, Z.Q. Yu, Y.X. Zhao, and X.M. Lai: *J. Phys.: Conf. Ser.*, 2018, vol. 1063, p. 12034.
27. F. Ozturk, S. Toros, and S. Kilic, Evaluation of tensile properties of 5052 type aluminum-magnesium alloy at warm temperatures. Technical report, 2008.
28. Y. Liu, Z. Zhu, Z. Wang, B. Zhu, Y. Wang, and Y. Zhang: *Int. J. Adv. Manuf. Technol.*, 2018, vol. 96(9–12), pp. 4063–83.
29. Q. Dai, Y. Deng, H. Jiang, J. Tang, and J. Chen: *Mater. Sci. Eng. A*, 2019, vol. 766, pp. 138325.
30. Y. Jiang and X. Xiao: High-Temperature Tensile Deformation Behaviour of Aluminium Alloy 2024 and Prediction of Forming Limit Curves, in *IOP Conference Series: Materials Science and Engineering*, Institute of Physics Publishing, 2018, vol. 439, pp. 042030.
31. T. Soysal and S. Kou: *Acta Mater.*, 2018, vol. 143, pp. 181–97.
32. C. Xia and S. Kou: *Metall Mater. Trans. B.*, 2021, vol. 52B(1), pp. 460–69.
33. C. Xia and S. Kou: *Sci. Technol. Weld. Join.*, 2020, vol. 25(8), pp. 690–97.
34. ISO ISO, 6892-2: 2018 *Metallic Materials-Tensile Testing-Part 2: Method of Test at Elevated Temperature*, Geneva, Switzerland, ISO, 2018.

Publisher's Note Springer Nature remains neutral with regard to jurisdictional claims in published maps and institutional affiliations.